Chapter 10

Manipulating Electromagnetic Waves with Zero Index Materials

Shiyang Liu, Jialin Zhou, Ying Han, Xinning Yu, Huajin Chen and Zhifang Lin

Additional information is available at the end of the chapter

http://dx.doi.org/10.5772/66663

Abstract

Zero-index material is a typical metamaterial with an effective zero refractive index, possessing a variety of exotic electromagnetic properties and particular functionalities. We have considered two kinds of zero-index materials with the first one a nearly matched zero index made of magnetic metamaterial and the second one a radially anisotropic zero index. The magnetic metamaterial-based systems are shown to be significant in wavefront engineering and flexibly tunable by an external magnetic field and a temperature field. The radially anisotropic zero-index-based systems can remarkably enhance the omnidirectional isotropic radiation by enclosing a line source and a dielectric particle within a shell configuration. The physical origin lies in that the dielectric particle effectively rescatters the trapped anisotropic higher order modes and converts them into the isotropic 0th order mode radiated outside the system. The case for the system with the loss is then examined and the energy compensation with a gain particle is also demonstrated.

Keywords: zero index materials, magnetic metamaterials, multiple scattering theory, omnidirectional isotropic radiation, Mie theory

1. Introduction

Metamaterials are a kind of composite electromagnetic (EM) materials consisting of subwavelength "meta-atoms" with either electric or magnetic response or even both, which possess nearly arbitrary profile of effective permittivity ε and permeability μ in principle [1–3]. A great deal of novel and unique EM properties, not occurring in natural materials, such as negative refraction [4, 5], cloaking [6, 7], illusion [8], and subwavelength propagation [9, 10] are theoretically predicted and experimentally implemented from the microwave region to the optical region. Zero-index material (ZIM) is a typical metamaterial with effective zero

refractive index, including ε-near-zero [11–13], μ-near-zero [14, 15], or both ε and μ near zero, a matched ZIM (MZIM) [16–18], and even more generally the ZIM with anisotropy [19–21].

Due to the extraordinary refractive index of the ZIMs, a great variety of bizarre EM behaviors and potential applications based on ZIM have been extensively investigated and reported. It has been demonstrated both theoretically and experimentally that the ZIM can be used to squeeze the electromagnetic wave and make it tunnel through a deep subwavelength channel with arbitrary shape, serving as a highly efficient coupler between incoming and outgoing waveguides [11, 13, 22]. Due to the zero phase delay in the ZIM, the phase pattern of an EM wave can be flexibly engineered, enabling the wavefront shaping [16, 23, 24]. The ZIM can also be used to modify and enhance the directive emission with high efficiency [20, 25, 26]. Compact omnidirectional metamaterial antennas can also be designed based on the anomalous transmittance of ε-near-zero ultranarrow radial channels [27]. Interestingly, by incorporating dielectric defects into the MZIM or ε-near-zero material the transmission and reflection can be switched by delicately controlling the defects [16, 28, 29]. Later on, Luo et al. [30] have implemented nearly perfect bending waveguides with anisotropic ZIM, while Cheng et al. [19] have used another kind of anisotropic ZIM, a radially anisotropic ZIM (RAZIM), to combine multiple sources and acquire omnidirectional radiation.

The ZIMs are usually composed of the building blocks made of metallic materials or dielectric materials, or sometimes are supposed to homogeneous media with the desired parameters in theoretical research. Here, we first present another kind of metamaterials composed of building blocks made of ferrite materials with intrinsic magnetic response, which are accordingly called magnetic metamaterials. The effective electric permittivity ε_{eff} and magnetic permeability μ_{eff} can be tuned by an external magnetic field (EMF) or temperature due to the dependence of ferrite materials on EMF and temperature, thus providing us with more degrees of tunability. In addition, the permeability of ferrite material is a second rank tensor with nonzero off-diagonal elements, indicating the time-reversal-symmetry breaking nature in magnetic metamaterials [31]. As a result, nonreciprocal behaviors can be observed in such system, even for the geometrically symmetric ZIM made of magnetic metamaterial. Then, we will consider a composite system constructed by a RAZIM shell enclosing a dielectric rod inside, which is used to implement a strongly enhanced two-dimensional (2D) isotropic radiation with relatively high efficiency. In addition, different from the configuration with the gain particles inserted inside the MZIM [32], our proposal does not alter the structure of the RAZIM shell and keep its homogeneity, which makes it experimentally feasible.

The research content of the present chapter consists of two main parts. In the first part, we present the design of ZIM with magnetic metamaterials by optimizing the parameters of configuration. Then, by calculating the photonic band diagrams and retrieving the effective constitutive parameters we can confirm the implementation of the ZIM. After that, the field patterns are simulated to demonstrate the zero-phase delay of the ZIM and wavefront modulation by sculpturing typical outgoing interfaces. Finally, the effective refractive index is shown to be thermally controlled due to the dependence of the saturation magnetization of ferrite materials on the ambient temperature. In the second part, we demonstrate a remarkable enhancement of omnidirectional radiation with the RAZIM shell by surrounding the line source together with a particular particle. A rigorous theoretical approach is presented to

http://dx.doi.org/10.5772/66663

analyze the phenomenon and optimize the related parameters. Then, the influence of the loss is examined, which can be compensated by introducing a gain particle. Finally, all the results are summarized in the conclusion part.

2. ZIM made of magnetic metamaterials

Magnetic metamaterials concerned in present work consist of an array of ferrite rods arranged periodically in air with either square or triangular lattice. Actually, configurations with some randomness introduced to the system are similar in the long wavelength limit, provided that the filling ratio of the ferrite materials is the same. Single-crystal yttrium-iron-garnet (YIG) is a good candidate for designing magnetic metamaterials due to its extremely low loss. In particular, the magnetic permeability of ferrite materials is dependent on an EMF, allowing for the realization of magnetically manipulable negative-index materials [33]. Combining the time-reversal symmetry breaking nature under an EMF, the one-way waveguiding tunable by an external magnetic field has been realized as well [34–36]. Bi and coworkers have shown that the thermally tunable negative index can also be realized with the magnetic metamaterials around the Curie temperature T_c based on the ferrimagnetic-paramagnetic transition of ferrite material. However, due to the narrow temperature range for the Mn-Zn ferrite material used in their work, the tunability is highly limited. Differently, for the single-crystal YIG employed in present design an even wider temperature range is permitted so that the effective refractive index can be adjusted from negative to zero and then to positive [37], signifying a great possibility to realize the gradient negative-zero-positive index material (NZPIM) [38, 39] when an appropriate gradient temperature field is applied to the system.

2.1. Photonic band diagrams and effective-medium theory

To examine the eigenmodes of the magnetic metamaterials, we employ the multiple-scattering theory to calculate the photonic band diagrams, which is proved to be powerful for the systems consisting of nonoverlap spheres or circular cylinders [40–45]. As for the effective electric permittivity ε_{eff} and magnetic permeability μ_{eff}, we will present simply a coherent potential approximation based effective-medium theory to retrieve these two constitutive parameters [46]. First thing first, for definiteness we should give the magnetic permeability of the single-crystal YIG ferrite rods fully magnetized along the z direction, parallel to the rod axes, which is a second rank tensor given by [47]

$$\widehat{\mu} = \begin{pmatrix} \mu_r & -i\mu_\kappa & 0 \\ i\mu_\kappa & \mu_r & 0 \\ 0 & 0 & 1 \end{pmatrix}, \qquad \widehat{\mu}^{-1} = \begin{pmatrix} \mu'_r & -i\mu'_\kappa & 0 \\ i\mu'_\kappa & \mu'_r & 0 \\ 0 & 0 & 1 \end{pmatrix}, \tag{1}$$

with $\mu_r = 1 + \frac{\omega_m(\omega_0 - i\alpha\omega)}{(\omega_0 - i\alpha\omega)^2 - \omega^2}$, $\mu_\kappa = \frac{\omega_m\omega}{(\omega_0 - i\alpha\omega)^2 - \omega^2}$, $\mu'_r = \frac{\mu_r}{\mu_r^2 - \mu_\kappa^2}$, and $\mu'_\kappa = \frac{-\mu_\kappa}{\mu_r^2 - \mu_\kappa^2}$, where $\omega_0 = \gamma H_0$ is the resonance frequency with $\gamma = 2.8$ MHz/Oe the gyromagnetic ratio, H_0 is the sum of the EMF applied in the z direction and the shape anisotropy field [47], $\omega_m = 4\pi\gamma M_s$ is the characteristic frequency with $4\pi M_s = 1750$ G the saturation magnetization, and $\alpha = 3 \times 10^{-4}$ is the damping

coefficient of the single-crystal YIG. The electric permittivity of the single-crystal YIG ferrite rods is $\varepsilon_s = 25 + i3\times10^{-3}$. In the calculation of photonic band diagram, we set $\alpha = 0$ [31] and $\varepsilon_s = 25$ to obtain the eigenmodes. For the 2D system, the transverse electric (TE) mode and the transverse magnetic (TM) mode are decoupled and we consider only the TM mode with the electric field polarized along the rod axis. In this case, the magnetic field of the incident wave is perpendicular to the EMF so that the magnetic field will interact with the precessing magnetic dipoles of the ferrite, thus leading to the control of an EMF on the magnetic permeability.

To calculate the eigenmodes and simulate the electric field patterns, we illustrate here how the multiple scattering theory is used to serve the purpose. For an incident TM wave, the electric field impinging to the ith ferrite rod can be expanded in terms of the vector cylindrical wave functions

$$\boldsymbol{E}_{\text{inc}} = E_0 \sum_m p_m J_m(k_0 r_i)\, e^{im\phi_i} \boldsymbol{e}_z, \tag{2}$$

where E_0 is the amplitude of the electric field, $J_m(k_0 r_i)$ is the mth order cylindrical Bessel function, k_0 is the wavenumber in the vacuum, $\boldsymbol{r}_i$ is the position vector of the polar angle ϕ_i in the coordinate system with the origin at the ith ferrite rod, $\boldsymbol{e}_z$ is the unit vector along rod axis, p_m is the expansion coefficient for the mth order partial wave of an incident field. The total scattering electric field can also be obtained by summarizing the scattering electric field from all the ferrite rods

$$\boldsymbol{E}_{sca} = -E_0 \sum_{i=1}^{N} \sum_{m=-m_c}^{m_c} b_m^{(i)} H_m^{(1)}(kr_i) e^{im\phi_i} \boldsymbol{e}_z, \tag{3}$$

where m_c is the critical angular momentum in the simulation to ensure the numerical convergence, N is the number of the ferrite rods, $H_m^{(1)}(kr_i)$ is the mth order Hankel function of the first kind, $b_m^{(i)}$ is the mth order scattering coefficient for the ith ferrite rod, which can be obtained according to

$$b_m^{(i)} = t_m^{(i)} \left[p_m^{(i)} - \sum_{j\neq i} \sum_n S_{mn}(i,j) b_n^{(j)} \right], \tag{4}$$

where $S_{mn}(i,j)$ is the structural factor that transforms the scattered wave from the jth ferrite rod into the incident wave on the ith ferrite rod and $t_m^{(i)}$ is the Mie-scattering coefficient of the ith ferrite rod, which was obtained exactly in literature [48].

$$t_m = \frac{\frac{\mu_s}{\mu_b} J'_m(x) - J_m(x)\left[\frac{m_s^2}{m'_s} D_m(m'_s x) + \frac{m\mu'_k}{x}\right]}{\frac{\mu_s}{\mu_b} H_m^{(1)'}(x) - H_m^{(1)}(x)\left[\frac{m_s^2}{m'_s} D_m(m'_s x) + \frac{m\mu'_k}{x}\right]}, \tag{5}$$

In Eq. (5), $J_m(x)$ and $H_m(x)$ are, respectively, the Bessel function and the Hankel function of the first kind, the superscript '" represents the derivative with respect to $x = k_b r_s$ with r_s the radius of the ferrite rod, $k_s^2 = \omega^2 \varepsilon_s \mu_s$, $m_s = k_s/k_b$, $m'_s = m_s/\sqrt{\mu'_r}$, and $D_n(m_{s'} x) = J'_n(m_{s'} x)/J_n(m_{s'} x)$.

Actually, there exist $N\times(2m_c+1)$ scattering coefficients for the whole system, corresponding to $N\times(2m_c+1)$ linear equations, which is the kernel part of the multiple scattering theory. In matrix form, the linear equations can be cast into

$$(\mathcal{S}+t^{-1})b=p. \tag{6}$$

The magnetic field can be derived easily from Maxwell's equations. To calculate the photonic band diagram, we should set $p = 0$ to solve the stationary-state equations so that the eigenfrequencies corresponding to the wavevectors in reduced Brillouin zone can be obtained.

For convenience, we recapitulate the results for the effective-medium theory; more details are referred to the published literature [46]. The scenarios of the effective-medium theory are as follows: (1) transform the periodic lattice of the magnetic metamaterials into the effective medium with effective constitutive parameters ε_{eff} and μ_{eff}; (2) take the unit cell of the magnetic metamaterials as an equal-area coated rod with ferrite rod as the inner core and the background medium as the coated layer with radius r_0, which is evidently an approximation, applicable only for the lattice with high symmetry. For a square lattice the radius $r_0=\frac{a}{\sqrt{\pi}}$, while for a hexagonal lattice the corresponding radius of the coated layer is $r_0=\sqrt[4]{3}\frac{}{\sqrt{2\pi}}a$; (3) the effective constitutive parameters ε_{eff} and μ_{eff} are determined by the condition that the total scattering of this coated rod in the effective medium vanishes in the long wave limit, namely, $k_0r_0\ll1$ and $k_0\sqrt{\varepsilon_{\text{eff}}}\sqrt{\mu_{\text{eff}}}\ll1$. After some mathematical manipulations, we can obtain the simplified equations determining the effective electric permittivity ε_{eff} and the effective magnetic permeability μ_{eff}.

$$\varepsilon_{\text{eff}}=(1-f)\varepsilon_0+f\tilde{\varepsilon}_s,\qquad \frac{\mu_{\text{eff}}-\mu_0}{\mu_{\text{eff}}+\mu_0}=f\,\frac{\tilde{\mu}_s-\mu_0-\xi}{\tilde{\mu}_s+\mu_0+\xi}, \tag{7}$$

where f is the filling fraction with $f=r_s^2/r_0^2$, and

$$\begin{gathered}\tilde{\varepsilon}_s=2\varepsilon_sF_2(x_s),\quad \tilde{\mu}_s=\mu_sG_2(x_s),\quad \xi=-\frac{(1-f)\mu_0^2(\mu_\kappa/\mu_r)^2(\tilde{\mu}_s/\mu_s)^2}{(1-f)\mu_0+(1+f)\tilde{\mu}_s},\\ F_2(x_s)=J_1(x_s)/[x_sJ_0(x_s)],\quad G_2(x_s)=J_1(x_s)/[x_sJ'_1(x_s)],\end{gathered} \tag{8}$$

with $x_s=k_sr_s$. It is noted that for the isotropic dielectric rod μ_κ is equal to zero, then Eq. (7) can be recovered to that for the isotropic metamaterials [49].

2.2. Phase patterns and wavefront engineering

By use of multiple-scattering theory, we calculate the photonic band diagrams for the magnetic metamaterials composed of the single-crystal YIG ferrite rods of the radius $r_s=3.3$ mm and arranged periodically with square lattice with the lattice separation $a=10$ mm. The results are shown in **Figure 1(a)** and **(c)**, corresponding, respectively, to the magnetic metamaterials under the EMF $H_0=510$ Oe and $H_0=460$ Oe. It can be found that there appear no eigenmodes below the first band, suggesting the formation of the photonic band gap. The first band possesses the negative slope, namely, $\mathrm{d}\omega/\mathrm{d}k<0$, corresponding to the negative ε_{eff} and μ_{eff}

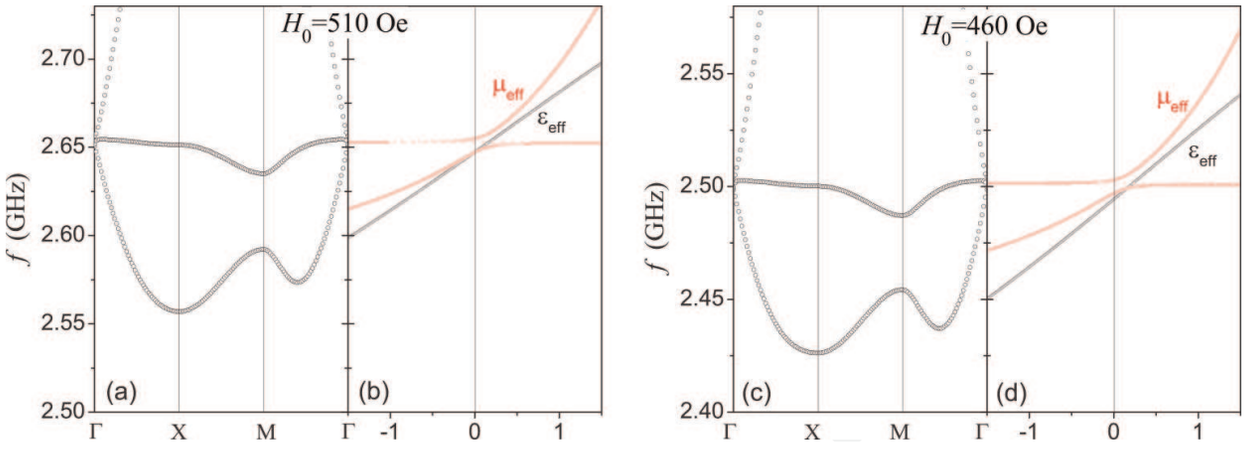

Figure 1. The photonic band diagrams for the magnetic metamaterials of square lattice under the EMF (a) $H_0 = 510$ Oe and (c) $H_0 = 460$ Oe, respectively. The corresponding effective electric permittivity ε_{eff} and magnetic permeability μ_{eff} are given in panels (b) and (d), respectively. The lattice separation is $a = 10$ mm and the radius of the ferrite rod is $r_s = 3.3$ mm.

as further corroborated by the effective constitutive parameters shown in **Figures 1(b)** and **(d)**. In particular, the first, second, and the third bands are degenerated at Γ point; meanwhile, the second band is nearly flat, signifying the characteristic of longitudinal mode. This accidental degeneracy can lead to the appearance of effective zero index with $\varepsilon_{\text{eff}} = \mu_{\text{eff}} = 0$ as confirmed by the effective-medium theory for the magnetic metamaterials under the EMF $H_0 = 510$ at the working frequency $f_w = 2.65$ GHz. Actually, the first and third bands form a Dirac cone at Γ point, which is consistent with that found by Huang et al. [16]. Interestingly, around the Dirac cone, the effective constitutive parameters ε_{eff} and μ_{eff} experience a nearly linear transition from negative to zero and then to positive except that a very narrow magnetic resonance appears, which is the difference of the magnetic metamaterials from the dielectric photonic crystals. This might be significant for investigating the EM features of NZPIM in frequency domain [50, 51]. More importantly, by decreasing the EMF from $H_0 = 510$ to 460 Oe both the photonic band diagram and the associated effective constitutive parameters are shifted downwards. As a result, the working frequency for the zero index is shifted from $f_w = 2.65$ to $f_w^{'} = 2.5$ GHz, suggesting the flexible tunability of the ZIM by an EMF. This offers us the opportunity to realize the NZPIM in space domain [38, 39] by applying a gradient EMF on magnetic metamaterials.

From the photonic band diagrams and the effective constitutive parameters ε_{eff} and μ_{eff}, we have obtained a good MZIM at the working frequency $f_w = 2.65$ GHz for the magnetic metamaterials under the EMF $H_0 = 510$ Oe. To examine the performance of the MZIM, the electric field pattern inside the MZIM can be simulated as shown in **Figure 2** for an MZIM slab illuminated by a Gaussian beam normally from the left-hand side. It can be found that although the thicknesses of three MZIM slabs are different, the phases of the outgoing beams are almost the same, showing nearly no change compared to that at the left interface. Inside the MZIM slab, the Gaussian beam experiences nearly no phase delay and electric field is nearly homogeneous, indicating the characteristic of the ZIM. In addition, the amplitude of the outgoing beam is comparable to that of the incident beam, indicating the impedance match of the MZIM with the air. Compared to the MZIM based on the dielectric photonic crystals the

http://dx.doi.org/10.5772/66663

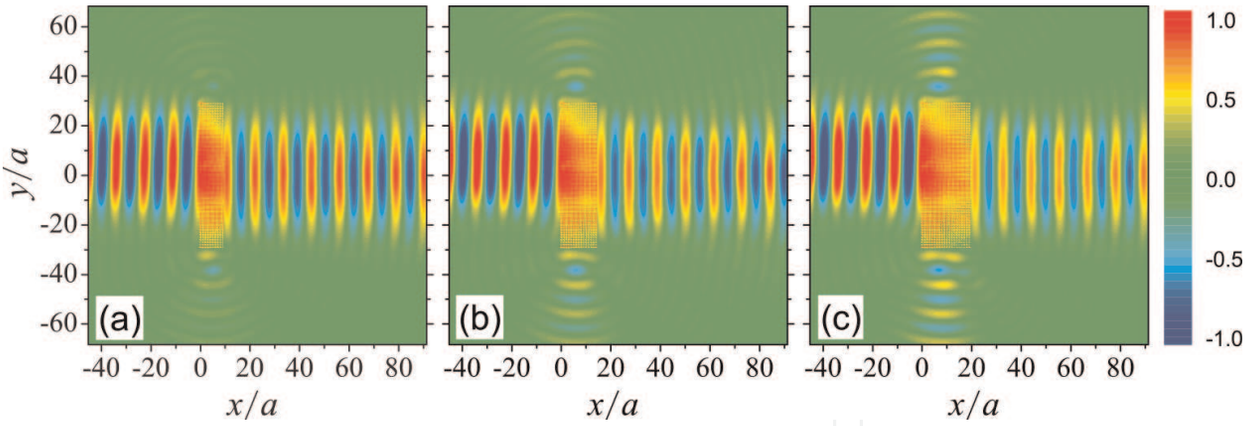

Figure 2. The electric field patterns of a Gaussian beam incident from the left-hand side of the ZIM slabs with the left interface fixed at $x = 0$ and the thickness of the slab $d_1 = 10a$ (a), $d_2 = 15a$ (b), and $d_3 = 20a$ (c), respectively. The height of the slab $D = 60a$, the working frequency is $f_w = 2.65$ GHz, and the other parameters are the same as those in Figure 1 (a) and (b).

coupling efficiency in present system is much higher, which originates from the anisotropy of the magnetic metamaterials as well as the subwavelength scale of the configuration. But for the dielectric photonic crystals the lattice separation is comparable to the working wavelength, implying a strong inhomogeneity. Anyhow, we can still observe some reflection due to the parallel momentum mismatch of the incident Gaussian beam at the interface. By calculating the reflectance and transmittance, we find that the reflectance becomes larger with the increase of the thickness, corresponding to 11.6, 18.9, and 24.1% for three different MZIM slabs. Differently, for a normal incident plane wave the reflectance is not larger than 1%, consistent with the above analysis. The transmittance for three different MZIM slabs are 84.3, 71.3, and 59.1%, less than 1 when adding to the reflectance, which comes from leaking of the EM energy from the upper and lower interface of the MZIM slabs as shown in **Figure 2**. Another interesting part is the upper shift of the reflection beam, corresponding to the nonreciprocal Goos-Hänchen shift, which deserves a further investigation in future work.

A particular functionality of the ZIM is to tailor the wavefront of the incident EM wave due to the zero phase delay inside the ZIM. We demonstrate such property by designing four typical outgoing interfaces sculptured from the MZIM, which are used to manipulate the wavefront of an incident Gaussian beam. The results are shown in **Figure 3**, where we can observe that the convex cylindrical face can transform the plane wavefront into the cylindrical one as shown in panel (a), different from the conventional convex lens that focuses the incident beam. It should be noted that the inhomogeneity of the outgoing beam arises from the anisotropy of the magnetic metamaterials. On the contrary, the concave cylindrical face can be used to focus the incident beam as shown in panel (b), behaving like a conventional convex lens but not a concave lens. The triangular prism can be used to split the incident beam into two separated ones propagating perpendicularly to the outgoing interfaces. More generally, we have shown in panel (d) an ordinary undulated interface that transforms the wavefront into the one identical to the interface. Actually, more imaginable configurations can be designed to engineer the wavefront in practice. In addition, the effective index of the magnetic metamaterials

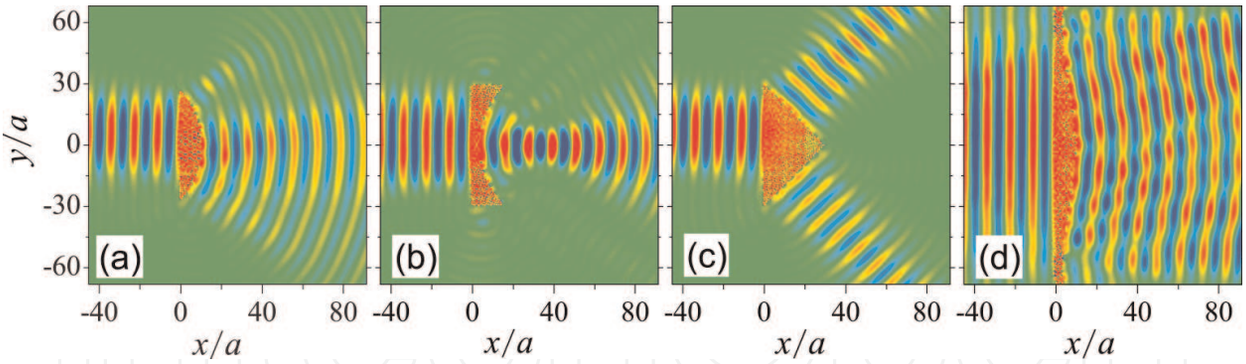

Figure 3. Wavefront engineering with different outgoing interfaces (a) convex cylindrical face, (b) concave cylindrical face, (c) triangular prism, and (d) ordinary undulated face. The radius of the curvature is 40a for panels (a) and (b), the waist radius of the incident Gaussian beam is 2λ for panels (a)–(c) and 6λ for (d). All the other parameters are the same as those in Figure 2.

can be controlled flexibly by an EMF, which can be used to transform the functionality of the above systems, for example, from focusing to defocusing or in an opposite manner.

2.3. Thermally controllable effective index

Another important property of ferrite materials is its saturation magnetization that is dependent on temperature, which can also be handled to control the EM properties of magnetic metamaterials. Single-crystal YIG bears a high Curie temperature $T_c = 523$ K, allowing a wide controlling temperature range and thus a better tunability on effective refractive index. The temperature field ranging from 0 (273.15 K) to 100°C (373.15 K) is considered for the magnetic metamaterials of triangular lattice with the lattice separation a = 10 mm and the rod radius $r_s = 3.4$ mm.

To examine the thermal effect on the magnetic metamaterials, we keep $H_0 = 485$ Oe unchanged, and tune the temperature T. The effective constitutive parameters ε_{eff} and μ_{eff} are presented in **Figure 4(a)–(c)**, respectively, under three different temperatures 306, 335, and 362

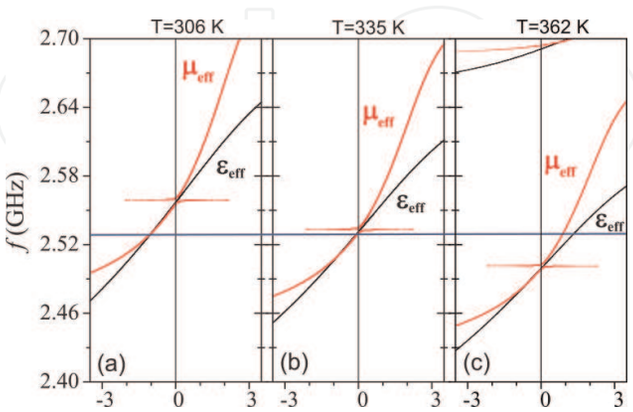

Figure 4. The real part of the retrieved effective electric permittivity ε_{eff} and magnetic permeability μ_{eff} for the magnetic metamaterials under three different temperatures (a) $T = 306$ K, (b) $T = 335$ K, and (c) $T = 362$ K, respectively. The lattice separation is a = 10 mm, the rod radius is $r_s = 3.4$ mm, and the EMF is $H_0 = 485$ Oe. The blue solid line marks the operating frequency $f_w = 2.53$ GHz.

K, corresponding to the saturation magnetization $4\pi M_s$ equal to 1740, 1650, and 1550 G. It should be noted that in our concerned frequency range $0.08 \leq \frac{a}{\lambda} \leq 0.09$, satisfying the long-wavelength approximation. As is shown in **Figure 4(a)**, under the temperature T = 306 K a nearly matched negative-index material with $\varepsilon_{\text{eff}} = \mu_{\text{eff}} = -1$ is obtained at the working frequency $f_w = 2.53$ GHz as marked by blue solid line. By improving the temperature, the curves of the effective constitutive parameters are shifted downwards as exhibited by comparing panels (a)–(c) due to the decrease of the saturation magnetization. Under the temperature $T = 362$ K, the effective electric permittivity $\varepsilon_{\text{eff}} = 1.36$ and the effective magnetic permeability $\mu_{\text{eff}} = 0.9$ are shown in **Figure 4(c)**, corresponding to a positive refractive index $n_{\text{eff}} = 1.1$. In particular, in between these two temperatures the effective electric permittivity $\varepsilon_{\text{eff}} = 0$ and the effective magnetic permeability $\mu_{\text{eff}} = -0.04$ close to zero under the temperature $T = 335$ K, resulting in the design of MZIM. As a result, a nearly continuous tuning of the effective constitutive parameters from negative to zero and then to positive is realized, suggesting that an NZPIM in space can be possibly implemented by the magnetic metamaterials under a gradient temperature field.

With the above knowledge, we can examine the performance of the magnetic metamaterials for molding EM wave propagation by simulating the field patterns of a TM Gaussian beam incident normally on a triangular prism with the apex angle $\theta = 90$. The results are shown in **Figure 5**, where we can observe that under the temperature $T = 306$ K the incident Gaussian beam is split into two separated beams propagating with the refractive angle $\theta_{\text{ref}} = 45$ as shown in panels (a) and (e), equal to the incident angle θ_{inc}, implying that the effective index of the triangular prism is $n_{\text{eff}} = -1$, consistent with the results from effective-medium theory given in **Figure 4(a)**. Under the temperature $T = 335$ K the effective constitutive parameters $\varepsilon_{\text{eff}} = 0$ and $\mu_{\text{eff}} = -0.04$, corresponding nearly to an MZIM, the electric field exhibits an invariant phase inside the prism, resulting in two perpendicularly outgoing beams with the same phase at two lateral interfaces as shown in panels (b) and (f). With further increasing the temperature to $T = 362$ K, we obtain the effective constitutive parameters $\varepsilon_{\text{eff}} = 1.36$ and $\mu_{\text{eff}} = 0.9$, corresponding to the effective index $n_{\text{eff}} = 1.1$, the Gaussian beam experiences a little bit focusing and collimation as shown in panels (c) and (g). When the temperature reaches $T = 367$ K, the effective constitutive parameters $\varepsilon_{\text{eff}} = 1.75$ and $\mu_{\text{eff}} = 1.11$, corresponding to the effective index $n_{\text{eff}} = 1.4$, a strong focusing with the outgoing beam waist radius shrunk nearly to λ can be observed as shown in panels (d) and (h).

3. Omnidirectional isotropic radiation via RAZIM

It has been shown that 2D RAZIM shell can be used to generate 2D isotropic radiation due to the fact that it can trap the anisotropic higher order modes, while it is transparent for the isotropic 0th order EM modes [19]. However, the efficiency is quite low since all the energy from the higher order modes are wasted, especially, when multiple sources are used since the energy of the higher order modes in that case occupies an even larger portion. We present an improved system with the 2D RAZIM shell enclosing a line source together with a conventional dielectric rod, which permits the generation of a perfect 2D EM mode; meanwhile, it is

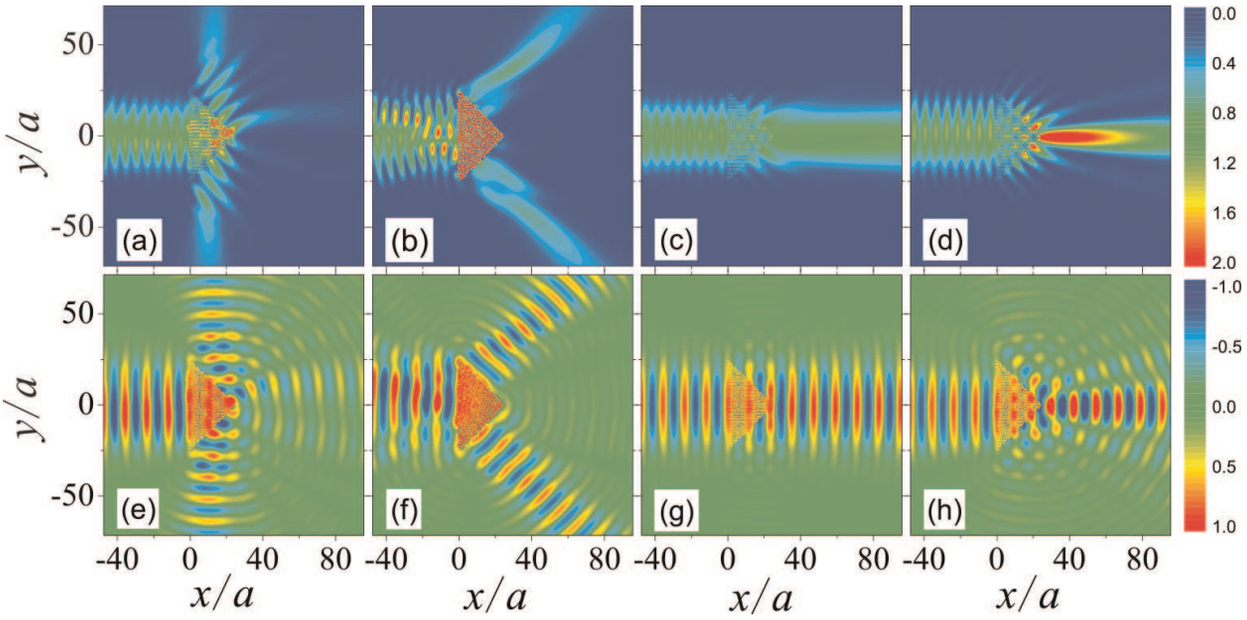

Figure 5. The electric field intensity $|E|^2$ (a)–(d) and electric field Re{E} (e)–(h) patterns for a Gaussian beam illuminating a triangular prism with the apex angle $\theta = 90°$ at the temperatures $T = 306$ K (a), (e); $T = 335$ K (b), (f); $T = 362$ K (c), (g); and $T = 367$ K (d), (h).

experimentally feasible. The dielectric rod can rescatter the anisotropic higher order EM modes and transform them into the isotropic 0th order modes. By positioning the dielectric rod at the strong field region of the anisotropic higher order modes, it can thus realize a great enhancement of omnidirectional radiation. The intrinsic loss of the RAZIM shell can also be examined and a gain-particle is used to compensate this dissipation.

3.1. Theoretical approach

The configuration of the system is schematically illustrated in **Figure 6**, where the shadowed green region is the RAZIM shell with a and b the inner and outer shell radii, and the dielectric rod and the line source are positioned inside the shell and denoted by D and S, respectively. In the cylindrical coordinate, the electric permittivity and magnetic permeability tensors of the RAZIM shell are characterized by [19, 52, 53]

$$\overline{\varepsilon} = \varepsilon_0(\hat{r}\hat{r}\varepsilon_r + \hat{\phi}\hat{\phi}\varepsilon_\phi + \hat{z}\hat{z}\varepsilon_z), \quad \overline{\mu} = \mu_0(\hat{r}\hat{r}\mu_r + \hat{\phi}\hat{\phi}\mu_\phi + \hat{z}\hat{z}\mu_z), \tag{9}$$

where $\mu_r \to 0$, corresponding to the radially anisotropic zero index. The origin of the cylindrical coordinate fixed at the center of the RAZIM shell. A line source of TM polarization is considered to interact with the RAZIM shell. For convenience, we first consider the simple system schematically illustrated in **Figure 6(a)** to depict the physical picture, based on which the system with further introducing a dielectric particle as shown in **Figure 6(b)** can be solved by further taking account of the mutual scattering between the dielectric particle and the RAZIM shell.

http://dx.doi.org/10.5772/66663

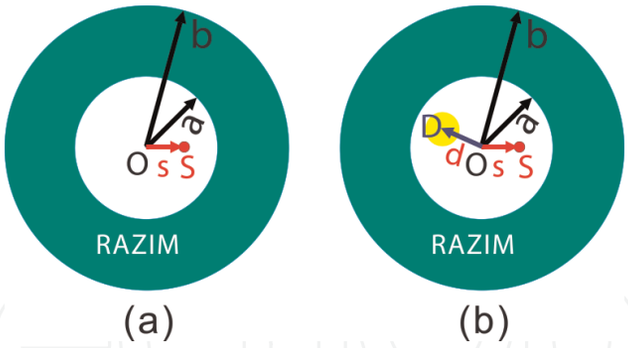

Figure 6. A schematic diagram illustrating the isotropic radiation system consisting of a RAZIM shell enclosing (a) a TM line source only and (b) both a TM line source and a dielectric rod of the radius r_d. The RAZIM shell center as well as the positions of the line source and the dielectric rod are denoted, respectively, by *O, S*, and *D* with $|OD| = d$ and $|OS| = s$. The background medium inside and outside the shell is vacuum. The inner and outer shell radii are a and b, respectively.

3.1.1. RAZIM shell enclosing only a single line source

In the framework of the generalized Lorenz-Mie theory, the EM field propagating in the RAZIM region can be expanded into the linear combination of the corresponding eigenmodes [19, 52]

$$E_z = \sum_m [B_m J_\nu(k_s r) + C_m H_\nu(k_s r)] e^{im\phi}, \quad a \le r \le b, \tag{10}$$

where $k_s^2 = k_0^2 \mu_\phi \varepsilon_z$ with k_0 the wavenumber in the vacuum, J_ν and H_ν are, respectively, the νth order Bessel functions and Hankel functions of first kind with the order $\nu = |m|\sqrt{\mu_\phi/\mu_r}$, and the summation m runs from $-\infty$ to ∞. The corresponding magnetic field in the transverse *xoy* plane can be obtained from Maxwell equations

$$H_r = \frac{1}{i\omega\mu_0\mu_r}\frac{1}{r}\frac{\partial E_z}{\partial \phi}, \quad H_\phi = -\frac{1}{i\omega\mu_0\mu_\phi}\frac{\partial E_z}{\partial r}, \tag{11}$$

for the TM waves. The electric field radiated by a TM line source positioned at $\boldsymbol{l}_s$ can also be expanded around the RAZIM shell center [54, 55]

$$\begin{aligned} E_z &= H_0(k|\boldsymbol{r}-\boldsymbol{l}_s|) = \sum_m J_m(ks) H_m(kr) e^{im\phi}, \quad r > s, \\ E_z &= H_0(k|\boldsymbol{r}-\boldsymbol{l}_s|) = \sum_m H_m(ks) J_m(kr) e^{im\phi}, \quad r < s, \end{aligned} \tag{12}$$

where $\boldsymbol{r}$ is the position vector and $s = |\boldsymbol{l}_s|$ is the separation between the line source and the RAZIM shell center. For convenience and without loss of generality, the line source is supposed to be located at (x_s, y_s) with $y_s = 0$, namely, the line source can be moved along the x axis. With these expansions, we can write the total electric field in different regions according to

$$\begin{aligned} E_z &= \sum_m [A_m J_m(kr) + J_m(ks) H_m(kr)] e^{im\phi}, \quad s < r \le a, \\ E_z &= \sum_m D_m H_m(kr) e^{im\phi}, \qquad\qquad\qquad\quad r \ge b, \end{aligned} \tag{13}$$

where the coefficients A_m characterize the reflection of mth order partial wave from the RAZIM shell, and D_m describes the transmission of the mth order partial wave radiating out of the shell.

By matching the boundary conditions, namely, the continuity of the tangential components of the EM field E_z and H_ϕ at the interface, we can work out the partial wave expansion coefficients for the EM fields in different regions,

$$B_m = q_m C_m, \qquad D_m = p_m C_m, \tag{14a}$$

$$A_m = q'_m J_m(ks), \qquad C_m = p'_m J_m(ks), \tag{14b}$$

where the generalized Mie coefficients are given by

$$p_m = \frac{k_s H_\nu(k_s b) J'_\nu(k_s b) - k_s H'_\nu(k_s b) J_\nu(k_s b)}{k_s H_m(kb) J'_\nu(k_s b) - k\mu_\phi H'_m(kb) J_\nu(k_s b)}, \tag{15a}$$

$$q_m = \frac{k\mu_\phi H_\nu(k_s b) H'_m(kb) - k_s H'_\nu(k_s b) H_m(kb)}{k_s H_m(kb) J'_\nu(k_s b) - k\mu_\phi H'_m(kb) J_\nu(k_s b)}, \tag{15b}$$

$$p'_m = \frac{k\mu_\phi H_m(ka) J'_m(ka) - k\mu_\phi H'_m(ka) J_m(ka)}{k\mu_\phi [H_\nu(k_s a) + q_m J_\nu(k_s a)] J'_m(ka) - k_s [H'_\nu(k_s a) + q_m J'_\nu(k_s a)] J_m(ka)}, \tag{15c}$$

$$q'_m = \frac{k_s H_m(ka) [H'_\nu(k_s a) + q_m J'_\nu(k_s a)] - k\mu_\phi H'_m(ka) [H_\nu(k_s a) + q_m J_\nu(k_s a)]}{k\mu_\phi [H_\nu(k_s a) + q_m J_\nu(k_s a)] J'_m(ka) - k_s [H'_\nu(k_s a) + q_m J'_\nu(k_s a)] J_m(ka)}. \tag{15d}$$

Regarding the RAZIM shell considered in our system, $\mu_r \to 0$, implying that the order ν of the cylindrical functions J_ν and H_ν in Eqs. (10), (13), and (15) tends to infinity for $m \neq 0$. As a result, $|H_\nu| \to \infty$ and $|J_\nu| \to 0$, leading to the vanishment of the Mie coefficient p'_m for $m \neq 0$. Therefore, it follows from Eq. (14) that $B_m \to 0$, $C_m \to 0$, and $D_m \to 0$ for $m \neq 0$. This indicates that the permitted propagating EM waves in the RAZIM shell are nearly independent of the azimuthal angle ϕ, as demonstrated by Eqs. (10) and (13). In addition, for the case when $\varepsilon_z = \mu_\phi = 1$, the Mie coefficients $p_0 = p'_0 = 1$, $q_0 = q'_0 = 0$, and $D_0 = J_0(kd)$. As a consequence, only the 0th order of the isotropic cylindrical EM wave can be radiated out of the RAZIM shell, ensuring its omnidirectionality, in agreement with the results obtained by Cheng et al. [19]. However, all the higher order modes of the cylindrical waves are confined within the RAZIM shell, hence, the RAZIM shell behaves like a cavity for these modes. Accordingly, the introduction of the RAZIM shell leads to the decrease of radiation power and reduces the radiation efficiency, although it can implement the spatial power combination for omnidirectional radiation.

Another important aspect for the RAZIM shell comes in the fact that it forms a cylindrical resonator for the higher order modes, which results in the creation of the standing wave with strong inhomogeneity inside the RAZIM shell. This particular feature arises from the anisotropy of the RAZIM shell, which is an essential aspect for the realization of isotropic radiation pattern. Besides, it is shown the RAZIM shell can be experimentally realizable both in microwave region [19] and in terahertz region [56], implying promising applications in future.

3.1.2. RAZIM shell enclosing a single line source together with a dielectric rod

To improve the radiating efficiency for the system shown in **Figure 6(a)**, we have to transform the higher order modes confined within the RAZIM shell into the isotropic lower order mode, and then radiating outside the RAZIM shell. To this end, a dielectric particle D can be introduced inside the RAZIM shell as illustrated in **Figure 6(b)**, which can rescatter the EM wave so that a part of the higher order modes can be converted into isotropic 0th order mode, thus enhancing the omnidirectional isotropic radiation from the RZAIM-shell-based system. Therefore, in this part we have to incorporate the contribution of the dielectric rod into theoretical framework. As is certain, the dielectric rod will change the scattering field inside central area surrounded by the shell and that propagating inside the shell. Therefore, the partial wave expansion coefficients A_m and C_m in Eq. (14b) should be altered

$$A_m = q'_m[J_m(ks) + E_m], \quad C_m = p'_m[J_m(ks) + E_m], \tag{16}$$

where E_m are the partial wave expansion coefficients of the scattered EM field from the dielectric rod D. As a result, the partial wave expansion coefficients B_m, and D_m are altered accordingly as indicated by Eq. (14a). It should be noted that the coefficients p_m, q_m, p'_m, and q'_m that characterize the scattering property of the RAZIM shell remain unchanged due to the fact that the RZAIM shell is intact when the dielectric rod D is introduced.

To consider the scattering behavior of the dielectric rod and obtain E_m, we should transform the expanding partial waves from the shell center to those from the dielectric rod D. The electric field inside the dielectric rod E_z^i and scattered by the rod E_z^s can be expanded easily into

$$E_z^i = \sum_m T_m J_m(k|\boldsymbol{r}-\boldsymbol{l}_d|)e^{im\phi}, \quad |\boldsymbol{r}-\boldsymbol{l}_d| < r_d, \tag{17a}$$

$$E_z^s = \sum_m S_m H_m(k|\boldsymbol{r}-\boldsymbol{l}_d|)e^{im\phi}, \quad |\boldsymbol{r}-\boldsymbol{l}_d| > r_d, \tag{17b}$$

where $\boldsymbol{l}_d$ is the position of the dielectric rod with $d = |\boldsymbol{l}_d|$ denoting the separation between the dielectric rod and the RAZIM shell center and r_d is the radius of the dielectric rod D. The partial wave expansion coefficients T_m and S_m are given by

$$T_m = b_m(R_m + I_m), \quad S_m = a_m(R_m + I_m), \tag{18}$$

where a_m and b_m are the Mie coefficients of the dielectric rod, I_m and R_m correspond to the contribution from the line source and that scattered inside by the RAZIM shell

$$I_m = H_m(kl)e^{in\phi'}, \quad R_m = \sum_n A_{m+n}J_n(kd)e^{in\phi_c}, \quad S_m = \sum_n E_{m+n}J_n(kd)e^{in\phi_c}. \tag{19}$$

The parameters in Eq. (19) are defined as $\phi_c = \angle DOS$, $\phi' = \angle DSO$, and $l^2 = d^2 + s^2 - 2d\,s\cos\phi_c$ is the distances from the dielectric rod to the line source S with $l/\sin\phi_c = d/\sin\phi'$. The Mie coefficients a_m and b_m of the dielectric rod can be easily obtained from the Mie theory [57]

$$b_m = \frac{k\mu_d J'_m(kr_d)H_m(kr_d) - k\mu_d J_m(kr_d)H'_m(kr_d)}{k_d J'_m(k_d r_d)H_m(kr_d) - k\mu_d H'_m(kr_d)J_m(k_d r_d)}, \tag{20a}$$

$$a_m = \frac{k\mu_d J'_m(kr_d)J_m(k_d r_d) - k_d J_m(kr_d)J'_m(k_d r_d)}{k_d J'_m(k_d r_d)H_m(kr_d) - k\mu_d H'_m(kr_d)J_m(k_d r_d)}, \tag{20b}$$

where $k_d^2 = k_0^2\varepsilon_d\mu_d$ with ε_d and μ_d being the permittivity and permeability of dielectric rod, respectively. For a particular case when the RAZIM shell is removed from the system, the corresponding scattering from the shell disappears, leading to $R_m = 0$. Combining Eqs. (16), (18), and (19) and after some mathematical manipulations, we can finally arrive at a set of linear equations

$$\sum_n (1 - a_m q'_n)J_{n-m}(kc)e^{i(n-m)\phi_c}E_n = \sum_n a_m q'_n J_n(kd)J_{n-m}(kc)e^{i(n-m)\phi_c} + a_m I_m, \tag{21}$$

which determine the coefficients E_n For now, we have solved the scattering problem for the RAZIM systems in both **Figure 6(a)** and **(b)**, based on which we can gain insight into the physical mechanism of the phenomenon as well as the role of the RAZIM shell and surrounded dielectric rod, meanwhile, optimize the configuration to achieve a better radiation efficiency.

3.2. Amplifying radiation with dielectric particle

In the simulations and calculations in this part except otherwise specified, the parameters for the RAZIM shell are $a = 0.5$, $b = 1$, $\mu_r = 0.01$, $\mu_\phi = 1$, $\varepsilon_z = 1$, and those for the dielectric rod are $r_d = 0.15$, $\varepsilon_d = 2$, and $\mu_d = 1$. The wavelength of the line source is set as unit $\lambda = 1$. To characterize the higher order modes trapped inside the RAZIM shell, we simulate the electric field amplitude $|E_z|$ pattern for the RAZIM shell enclosing only a line source, the result is shown in **Figure 7(a)**, where the line source is fixed at (0.1, 0) deviated from the shell center so that the higher order modes can be excited. A standing wave with strong inhomogeneity emerges, which is created by the higher order partial waves in Eq. (12) due to the nearly total reflection from the RAZIM shell. The EM wave-radiating outside the RAZIM shell can be calculated approximately by $E_z \approx D_0 H_0(kr) = [J_0(ks) + E_0]H_0(kr)$. Therefore, the performance of the dielectric rod can be evaluated approximately by calculating the amplitude of $|D_0|$. The simulating result is shown in **Figure 7(b)**, where the map of $|D_0|$ as the function of the dielectric rod position (x_d, y_d) is plotted, based on which we can find the optimal position of the dielectric rod is near to the area with the strongest electric field amplitude. In addition, $|D_0|$ has a much

http://dx.doi.org/10.5772/66663

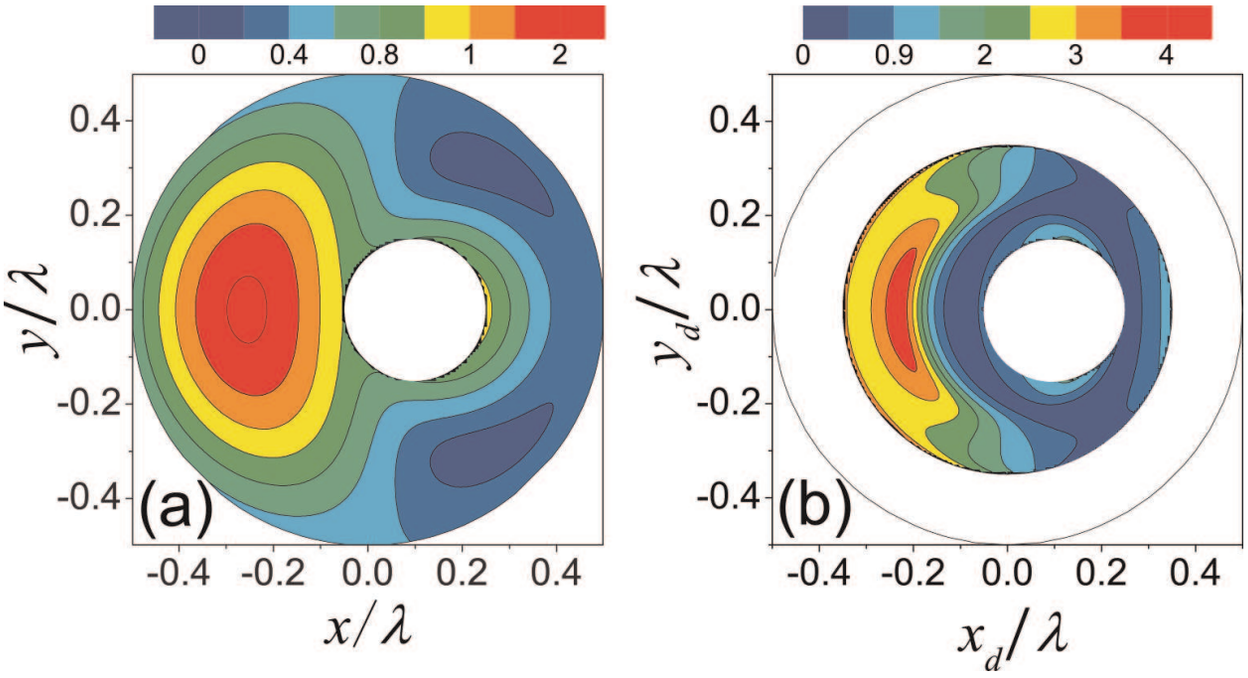

Figure 7. (a) The electric field amplitude pattern inside the RAZIM shell for the configuration in Figure 6(a). (b) The 0th order partial wave amplitude $|D_0|$ is plotted as the function of the dielectric rod position (x_d, y_d). The whiteout region in panel (b) denotes the area that the dielectric rod cannot reach. The line source is located at (0.1, 0), and the parameters of the RAZIM-based system are $a = 0.5$, $b = 1$, $r_d = 0.15$, $\mu_r = 0.01$, $\mu_\phi = 1$, $\varepsilon_z = 1$, $\varepsilon_d = 2$, and $\mu_d = 1$.

larger value than that of a free line source in a large area, indicating the crucial role of the dielectric rod for enhancing the isotropic radiation. Another merit of the present system lies in that the introduction of a dielectric rod inside the RAZIM shell does not destroy the homogeneity of the RAZIM shell, making it experimentally realizable.

To optimize the performance of the dielectric rod, we calculate the total power radiating out of the RAZIM shell, which is defined as

$$P_s = \oint_L \boldsymbol{S} \cdot \boldsymbol{e}_r \, \mathrm{d}l, \quad \text{with} \quad \boldsymbol{S} = \frac{1}{2}\mathrm{Re}[\boldsymbol{E} \times \boldsymbol{H}^*], \tag{22}$$

where $\boldsymbol{S}$ is the Pointing vector, the integral curve L is a circle around the shell center O with the radius larger than outer radius of the RAZIM shell b. Considering the fact that only the 0th order cylindrical wave is radiated out, the radiating power can be approximately evaluated according to $P_{wi} \approx \frac{2}{\omega\mu_0}|D_0|^2$. For the convenience of comparison, we also calculate the radiating power P_{wo} when the RAZIM shell is removed from the system $P_{wo} = \frac{2}{\omega\mu_0}\sum_m |a_m H_m(kl) + J_m(kl)|^2$. In **Figure 8**, we present the radiating power normalized by that of a line source in free space P_{s0} and the profile of the normalized irradiance by that of a line source in free space I_0. For the radiating power without the RAZIM shell P_{wo}/P_{s0}, its value exhibits nearly no change with respect to the dielectric rod position x_d as indicated by the blue dashed line in panels (a). Even when the dielectric rod is replaced by a gain particle, P_{wo}/P_{s0} remains close to 1, suggesting that without the RAZIM shell the insertion of either passive or active particle has nearly no obvious influence on the radiating power due to the nearly homogeneous distribution of a line

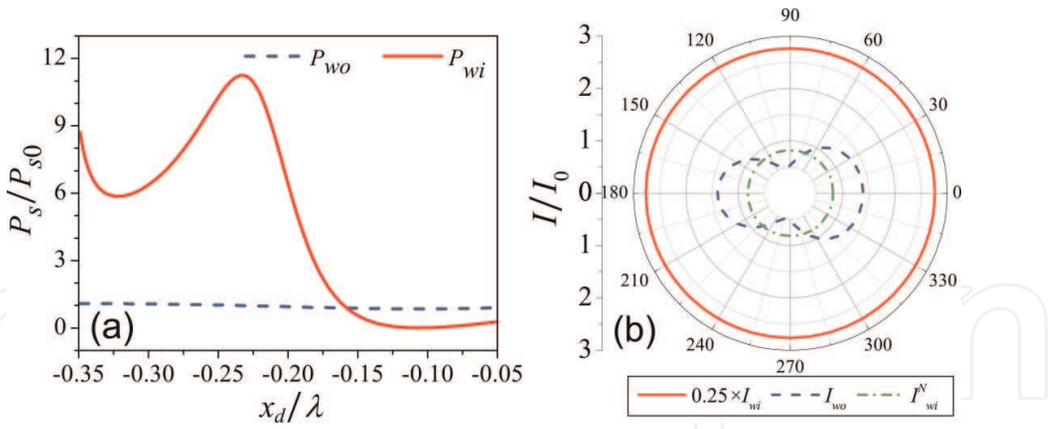

Figure 8. (a) The normalized radiating power P_s/P_{s0} is plotted as the function of the dielectric rod position x_d with the line source positioned at (0.1, 0), where the blue-dashed (red solid) line denotes the radiating power P_{wo} (P_{wi}) for the case without (with) the RAZIM shell. (b) The map of the normalized irradiance I/I_0, where the red solid line, the blue-dashed line, and the green dash-dotted line correspond to $I_{wi}/4$, I_{wo}, and I^N_{wi}, respectively, with $I_{wi}/4$ for the system with the RAZIM shell and the dielectric rod, I_{wo} for the system without the RAZIM shell, and I^N_{wi} for the system with RAZIM shell but without the dielectric rod D. The dielectric rod is placed at $(-0.24, 0)$ and all the other parameters are the same as those in Figure 7.

source in free space. Differently, for the radiating power with the RAZIM shell P_{wi}/P_{s0}, its value can be significantly improved as indicated by the red solid line shown in panels (a). The maximal enhancement is realized at the position close to the strongest electric field amplitude in **Figure 7(a)** with the value larger than 10. To illustrate the performance of the dielectric rod on the isotropic omnidirectional radiation, we present in **Figure 8(b)** the normalized irradiance by that of the line source in free space I_0 with the irradiance is defined as $I = \lim_{r\to\infty}(S \cdot r)$. From the irradiance profile for the system with the RAZIM shell I_{wi}, it can be found that the irradiance is reinforced by over 10 times as indicated by the red solid line, consistent with the result shown in **Figure 8(a)**. In addition, a highly isotropic feature is demonstrated as well by examining the irradiance map. For the convenience of comparison, we also present the irradiance I_{wo} for the system without the RAZIM shell as denoted by the blue dash line, which is not isotropic anymore and no evident enhancement is achieved with either the dielectric rod or the gain particle. The efficiency of the dielectric rod can be evaluated by comparing I_{wi} with the radiance I^N_{wi} for the case with the dielectric rod removed from the system. The profile of I^N_{wi} is denoted by the green dash-dot line, where we can find that only 80% EM energy of the line source is radiated out because of the trap of the high order modes by the RAZIM shell. This suggests that an insertion of a dielectric rod leads to a nearly 15 times amplification of the radiation power.

3.3. Amplifying radiation with gain particle

In practice, the loss should be an inevitable issue due to the finite size of the RAZIM shell and its resonant nature. To illustrate the effect of the loss on the radiation enhancement, we present in **Figure 9** the results for the system with the loss taken into account, where we can find that the output radiating power is reduced seriously compared to the results shown in **Figure 8**. To compensate the energy loss, the active coated nanoparticles might be a good choice. By

http://dx.doi.org/10.5772/66663

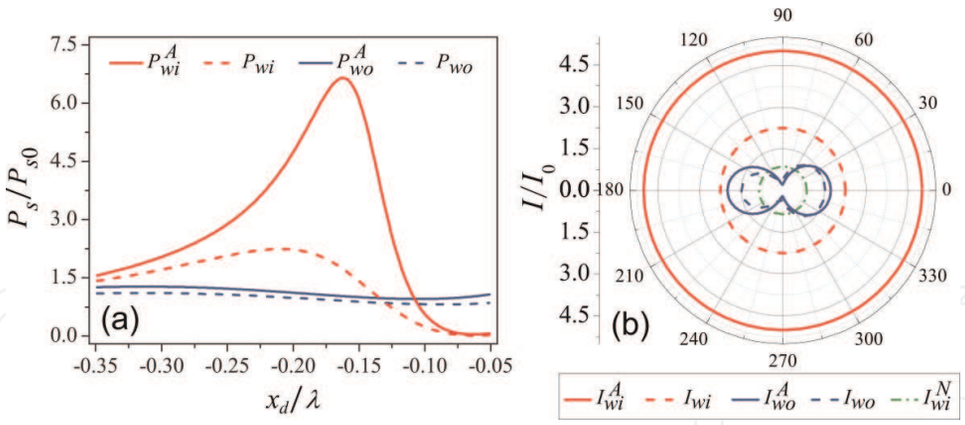

Figure 9. (a) The normalized radiating power P_s/P_{s0} is plotted as the function of the position x_d of the gain particle with $\varepsilon_d = 2.5–0.5i$ (solid lines) and the lossless dielectric particle with $\varepsilon_d = 2.5$ (dashed lines) for the system with (red lines) and without (blue lines) the RAZIM shell, respectively. The map of the normalized irradiance I/I_0 is shown in panel (b), where the red (blue) solid line corresponds to the result I_{wi}^A (I_{wo}^A) for the system with the gain particle modeled by $\varepsilon_d = 2.5–0.5i$ and with (without) the RAZIM shell, the red (blue) dashed line corresponds to the result I_{wi} (I_{wo}) for the system with the lossless dielectric particle of $\varepsilon_d = 2.5$ and with (without) the RAZIM shell, and the green dash-dotted line is for the system with the RAZIM shell but without the particle inside. The particle with the radius $r_d = 0.15$ is placed at $(-0.2, 0)$, the line source is positioned at (0.1, 0), $\mu_r = 0.01 + 0.005i$, $\mu_\phi = 1 + 0.005i$, and $\varepsilon_z = 2 + 0.005i$. All the other parameters are the same as those in Figure 6.

enclosing a gain particle with $\varepsilon_d = 2.5–0.5i$, we can compensate the energy loss from the RAZIM shell, yielding an enhancement of the output radiating power by a factor of about 7 as indicated by the red solid line in **Figure 9**. For comparison, the case for the system without the RAZIM shell but with a gain particle is also simulated as indicated by the blue solid line. Neither significant increase nor isotropy in the output radiation is achieved, suggesting once again the crucial role of the RAZIM shell.

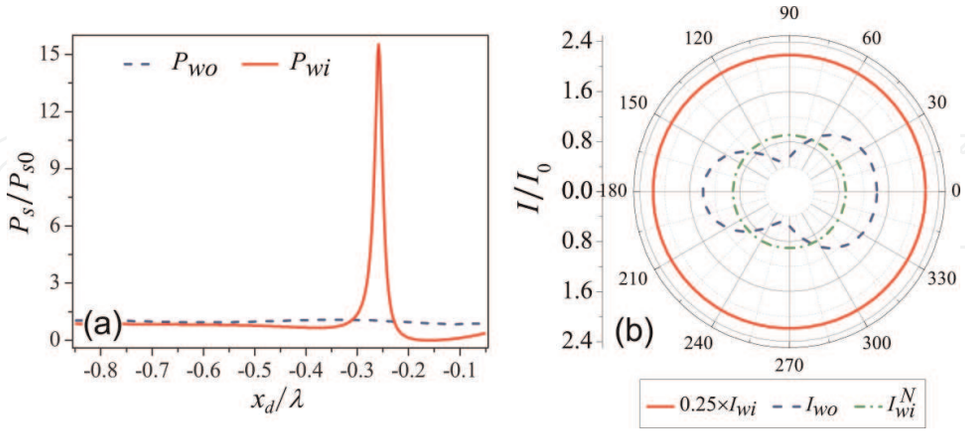

Figure 10. (a) The normalized radiating power P_s/P_{s0} is plotted as a function of the position x_d of the particle with $\varepsilon_d = 2$ for the system with (red solid line) and without (blue dashed line) the RAZIM shell, respectively. The map of the normalized irradiance I/I_0 is shown in panel (b), where the red solid (blue dashed) line corresponds to the result $0.25\times I_{wi}$ (I_{wo}) for the system with a lossless dielectric particle of $\varepsilon_d = 2.5$ and with (without) the RAZIM shell and the green dash-dotted line is for the system with the RAZIM shell but without the particle inside. The particle with the radius $r_d = 0.15$ is placed at $(-0.25, 0)$, the line source is fixed at (0.1, 0), $a = 1$, $b = 2$, $\lambda = 1$, $\mu_r = 0.001$, $\mu_\phi = 1$, and $\varepsilon_z = 1$.

The size of the RAZIM shell also has effect on the enhancement of the output radiation, which is illustrated in **Figure 10** for the RAZIM shell with $a = 1$ and $b = 2$. It can be found that the enhancement of the omnidirectional radiation becomes difficult in that only in a quite narrow range of the enhancement can be achieved as shown in **Figure 10(a)**. The underlying physics is as follows. Since the field due to the anisotropic higher order modes is trapped inside the RAZIM shell, the field is highly confined and anisotropic when the shell is small so that there appears the region with strong field easily. Then, a dielectric rod located near the position with strong field can rescatter the anisotropic modes into the isotropic mode, inducing a remarkable increase of the output radiating power. Differently, for large RAZIM shell, the anisotropic higher order modes are usually much less confined. As a result, the introduction of a dielectric rod cannot yield a strong rescattering of the trapped anisotropic modes into the isotropic field, resulting in a smaller enhancement of radiation power. Roughly speaking, the design works when the RAZIM shell is small. Nevertheless, the size of RAZIM shell is not necessarily limited to subwavelength scale. As shown in **Figure 10(b)** by the red solid line, a strong enhancement can still be achieved by a proper arrangement of the dielectric particle.

4. Conclusion

In summary, we have designed a kind of zero-index materials (ZIMs) with magnetic metamaterials based on the multiple scattering theory and effective-medium theory. The zero phase delay inside the ZIMs and the wavefront engineering are demonstrated. It is also shown that the effective index can be flexibly tuned by an external magnetic field and temperature, enabling the manipulation on the functionalities. In addition, the anisotropy of the ZIMs and the nonreciprocal feature of the magnetic metamaterials might induce nonreciprocal Goos-Hänchen and other physical consequences. Then, in the second part we have considered a radially anisotropic ZIM (RAZIM) based system with a RAZIM shell enclosing both a line source and a dielectric rod, which can implement a remarkably enhanced omnidirectional radiation. An exact theoretical approach is developed to solve the system, based on which we can optimize the configuration to achieve the high efficiency, more importantly, discover the underlying physics. Actually, the RAZIM shell allows only the 0-th order isotropic mode to radiate outside the system, ensuring the isotropy of the radiation. Differently, the anisotropic higher order modes are trapped, thus creating a strongly inhomogeneous standing wave. The dielectric rod can rescatter the anisotropic modes into isotropic one, enhancing the omnidirectional radiation remarkably. Besides, the present design is experimentally feasible, and meanwhile provides a highly efficient omnidirectional radiation by spatial power combination.

Acknowledgements

This work was supported by the China 973 Projects (No. 2013CB632701), the National Natural Science Foundation of China (Nos. 11274277, 11574055, and 11574275), MOE of China (B06011), the Zhejiang Provincial Natural Science Foundation of China (LR16A040001), and the open project of SKLSP (KF2016_3) in Fudan University.

Author details

Shiyang Liu[1]*, Jialin Zhou[1], Ying Han[1], Xinning Yu[2], Huajin Chen[2,3] and Zhifang Lin[2]

*Address all correspondence to: syliu@fudan.edu.cn

1 Institute of Information Optics, Zhejiang Normal University, Zhejiang, China

2 Surface Physics Laboratory, Department of Physics, Fudan University, Shangai, China

3 School of Electrical and Information Engineering, Guangxi University of Science and Technology, China

References

[1] Pendry JB. Negative refraction makes a perfect lens. Phys. Rev. Lett. 2000; **85**: 3966–3969.

[2] Shelby RA, Smith DR, Schultz S. Experimental verification of a negative index of reflection. Science. 2001; **292**: 77–79.

[3] Caiazzo M, Maci S, Engheta N. A metamaterial surface for compact cavity resonators. IEEE Antenn. Wireless Propag. Lett. 2004; **3**: 261–264.

[4] Shalaev VM. Optical negative-index metamaterials. Nat. Photon. 2007; **1**: 41–48.

[5] Valentine J, Zhang S, Zentgraf T, Ulin-Avila E, Genov DA, Bartal G, Zhang X. Three-dimensional optical metamaterial with a negative refractive index. Nature. 2008; **455**: 376–379.

[6] Leonhardt U. Optical conformal mapping. Science. 2006; **312**: 1777–1780.

[7] Pendry JB, Schurig D, Smith DR. Controlling electromagnetic fields. Science. 2006; **312**: 1780–1782.

[8] Lai Y, Ng J, Chen HY, Han DZ, Xiao JJ, Zhang ZQ, Chan CT. Illusion optics: the optical transformation of an object into another object. Phys. Rev. Lett. 2009; **102**: 253902.

[9] Maier SA, Kik PG, Atwater HA. Observation of coupled plasmon-polariton modes in Au nanoparticle chain waveguides of different lengths: estimation of waveguide loss. Appl. Phys. Lett. 2002; **81**: 1714–1716.

[10] Maier SA, Kik PG, Atwater HA, Meltzer S, Harel E, Koel BE, Requicha AAG. Local detection of electromagnetic energy transport below the diffraction limit in metal nanoparticle plasmon waveguides. Nat. Mater. 2003; **2**: 229–232.

[11] Edwards B, Alù A, Young M, Silveirinha M, Engheta N. Experimental verification of epsilon- near-zero metamaterial coupling and energy squeezing using a microwave waveguide. Phys. Rev. Lett. 2008; **100**: 033903.

[12] Garcia N, Ponizovskaya EV, Xiao JQ. Zero permittivity materials: band gaps at the visible. Appl. Phys. Lett. 2002; **80**: 1120–1122.

[13] Silveirinha MG, Engheta N. Tunneling of electromagnetic energy through subwavelength channels and bends using ε-near-zero materials. Phys. Rev. Lett. 2006; **97**: 157403.

[14] Jin Y, Zhang P, He SL. Squeezing electromagnetic energy with a dielectric split ring inside a permeability-near-zero metamaterial. Phys. Rev. B. 2010; **81**: 085117.

[15] Silveirinha MG, Belov PA. Spatial dispersion in lattices of split ring resonators with permeability near zero. Phys. Rev. B. 2008; **77**: 233104.

[16] Huang XQ, Lai Y, Hang ZH, Zheng HH, Chan CT. Dirac cones induced by accidental degeneracy in photonic crystals and zero-refractive-index materials. Nat. Mater. 2011; **10**: 582–586.

[17] Silveirinha MG, Engheta N. Design of matched zero-index metamaterials using nonmagnetic inclusions in epsilon-near-zero media. Phys. Rev. B. 2007; **75**: 075119.

[18] Ziolkowski RW. Propagation in and scattering from a matched metamaterial having a zero index of refraction. Phys. Rev. E. 2014; **70**: 046608.

[19] Cheng Q, Jiang WX, Cui TJ. Spatial power combination for omnidirectional radiation via anisotropic metamaterials. Phys. Rev. Lett. 2012; **108**: 213903.

[20] Yuan Y, Shen LF, Ran LX, Jiang T, Huangfu JT, Kong JA. Directive emission based on anisotropic metamaterials. Phys. Rev. A. 2008; **77**: 053821.

[21] Zhu WR, Rukhlenko ID, Premaratne M. Application of zero-index metamaterials for surface plasmon guiding. Appl. Phys. Lett. 2013; **102**: 011910.

[22] Liu RP, Cheng Q, Hand T, Mock JJ, Cui TJ, Cummer SA, Smith DR. Experimental demonstration of electromagnetic tunneling through an epsilon-near-zero metamaterial at microwave frequencies. Phys. Rev. Lett. 2008; **100**: 023903.

[23] Alù A, Silveirinha MG, Salandrino A, Engheta N. Epsilon-near-zero metamaterials and electromagnetic sources: tailoring the radiation phase pattern. Phys. Rev. B. 2007; **75**: 155410.

[24] Feng SM. Loss-induced omnidirectional bending to the normal in ε-near-zero metamaterials. Phys. Rev. Lett. 2012; **108**: 193904.

[25] Enoch S, Tayeb G, Sabouroux P, Guerin N, Vincent P. A metamaterial for directive emission. Phys. Rev. Lett. 2002; **89**: 213902.

[26] Ma YG, Wang P, Chen X, Ong CK. Near-field plane-wave-like beam emitting antenna fabricated by anisotropic metamaterial. Appl. Phys. Lett. 2009; **94**: 044107.

[27] Soric JC, Engheta N, Maci S, Alù A. Omnidirectional metamaterial antennas based on ε-near-zero channel matching. IEEE Trans. Antennas Propag. 2013; **61**: 33–44.

[28] Hao JM, Yan W, Qiu M. Super-reflection and cloaking based on zero index metamaterial. Appl. Phys. Lett. 2012; **96**: 101109.

[29] Nguyen VC, Chen L, Halterman K. Total transmission and total reflection by zero index metamaterials with defects. Phys. Rev. Lett. 2010; **105**: 233908.

[30] Luo J, Xu P, Chen HY, Hou B, Gao L, Lai Y. Realizing almost perfect bending waveguides with anisotropic epsilon-near-zero metamaterials. Appl. Phys. Lett. 2012; **100**: 221903.

[31] Wang Z, Chong YD, Joannopoulos JD, Soljačić M. Reflection-free one-way edge modes in a gyromagnetic photonic crystal. Phys. Rev. Lett. 2008; **100**: 013905.

[32] Zhu WR, Rukhlenko ID, Premaratne M. Light amplification in zero-index metamaterial with gain inserts. Appl. Phys. Lett. 2012; **101**: 031907.

[33] Liu SY, Chen WK, Du JJ, Lin ZF, Chui ST, Chan CT. Manipulating negative-refractive behavior with a magnetic field. Phys. Rev. Lett. 2008; **101**: 157407.

[34] Liu SY, Lu WL, Lin ZF, Chui ST. Magnetically controllable unidirectional electromagnetic waveguiding devices designed with metamaterials. Appl. Rev. Lett. 2010; **97**: 201113.

[35] Liu SY, Lu WL, Lin ZF, Chui ST. Molding reflection from metamaterials based on magnetic surface plasmons. Phys. Rev. B. 2011; **84**: 045425.

[36] Poo Y, Wu RX, Liu SY, Yang Y, Lin ZF, Chui ST. Experimental demonstration of surface morphology independent electromagnetic chiral edge states originated from magnetic plasmon resonance. Appl. Phys. Lett. 2012; **101**: 081912.

[37] Yu XN, Chen HJ, Lin HX, Zhou JL, Yu JJ, Qian CX, Liu SY. Continuously tuning effective refractive index based on thermally controllable magnetic metamaterials. Opt. Lett. 2014; **39**: 4643–4646.

[38] Ding YS, Chan CT, Wang RP. Optical waves in a gradient negative-index lens of a half-infinite length. Sci. Rep. 2013; **3**: 2954.

[39] Litchinitser NM, Maimistov AI, Gabitov IR, Sagdeev RZ, Shalaev VM. Metamaterials: electromagnetic enhancement at zero-index transition. Opt. Lett. 2008; **33**: 2350–2352.

[40] Li LM, Zhang ZQ. Multiple-scattering approach to finite-sized photonic band-gap materials. Phys. Rev. B. 1998; **58**: 9587–9590.

[41] Lin ZF, Chui ST. Electromagnetic scattering by optically anisotropic magnetic particle. Phys. Rev. E. 2004; **69**: 056614.

[42] Lin ZF, Chui ST. Manipulating electromagnetic radiation with magnetic photonic crystals. Opt. Lett. 2007; **32**: 2288–2290.

[43] Liu SY, Lin ZF. Opening up complete photonic bandgaps in three-dimensional photonic crystals consisting of biaxial dielectric spheres. Phys. Rev. E. 2006; **73**: 066609.

[44] Moroz A. Metallo-dielectric diamond and zinc-blende photonic crystals. Phys. Rev. B. 2002; **66**: 115109.

[45] Stefanou N, Yannopapas V, Modinos A. Heterostructures of photonic crystals: frequency bands and transmission coefficients. Comput. Phys. Commun. 1998; **113**: 49–77.

[46] Jin JJ, Liu SY, Lin ZF, Chui ST. Effective-medium theory for anisotropic magnetic metamaterials. Phys. Rev. B. 2009; **80**: 115101.

[47] Pozar DM. Microwave Engineering. New York: Wiley; 2004.

[48] Eggimann WH. Scattering of a plane wave on a ferrite cylinder at normal incidence. IRE Trans. Microwave Theory Tech. 1960; **8**: 440.

[49] Wu Y, Li J, Zhang ZQ, Chan CT. Effective medium theory for magnetodielectric composites: beyond the long-wavelength limit. Phys. Rev. B. 2006; **74**: 085111.

[50] Shen M, Ruan LX, Wang XL, Shi JL, Wang Q. Tunable band gap near the Dirac point in nonlinear negative-zero-positive index metamaterial waveguide. Phys. Rev. A. 2011; **83**: 045804.

[51] Yannopapas V, Vanakaras A. Dirac point in the photon dispersion relation of a negative/zero/positive-index plasmonic metamaterial. Phys. Rev. B. 2011; **84**: 045128.

[52] Ni YX, Gao L, Qiu CW. Achieving invisibility of homegeneous cylindrically anisotropic cylinders. Plamonics. 2010; **5**: 251-258.

[53] Wang N, Chen HJ, Lu WL, Liu SY, Lin ZF. Giant omnidirectional radiation enhancement via radially anisotropic zero-index metamaterial. Opt. Express. 2013; **21**: 23712.

[54] Abramowitz M, Stegun IA. Handbook of Mathematical Functions with Formulas, Graph, and Mathematical Tables. Dover; New York: 1964.

[55] Chew WC. Waves and Fields in Inhomogeneous Media. New York: IEEE Press; 1995.

[56] Chen ZC, Mohsen R, Gong YD, Chong TW, Hong MH. Realization of variable three-dimensional terahertz metamaterial tubes for passive resonance tunability. Adv. Mater. 2002; **24**: 143–147.

[57] Bohren CF, Huffman DR. Absorption and Scattering of Light by Small Particles. New York: John Wiley & Sons; 1983.